ATLAS CONF Note

ATLAS-CONF-2019-027

11th July 2019

Soft b-hadron tagging for compressed SUSY scenarios

The ATLAS Collaboration

b-hadrons with transverse momenta too low to yield a calorimeter jet that can be efficiently identified by b-tagging techniques are ubiquitous in scenarios of compressed spectra of supersymmetric third generation particles. Three different techniques to tag low transverse momentum b-hadrons are described and characterised. One of them makes use of jets reconstructed only from tracks, while the other two explore the feasibility and performance of a vertex reconstruction not relying on any jet finding. The approaches are found to be complementary, with the latter two yielding better sensitivity to b-hadron transverse momenta in the 5-15 GeV range, and the former providing the best performance above 15 GeV.

1 Introduction

The ability to identify b-hadrons in the data from the ATLAS detector, whose decay products leave a significant amount of energy in the calorimeters, has been repeatedly assessed [1, 2]. Such b-tagging techniques make use of the tracks associated to the calorimeter jet resulting from the hadronisation of a b-quark, and exploit observables correlated with the b-hadron lifetime and mass, such as the track impact parameters, the presence of a secondary decay vertex and the topology of the b-hadron decay.

The use of calorimeter jets as a starting point for b-tagging sets constraints on the energy that a b-hadron and surrounding hadronic activity must have. Standard b-tagging techniques in ATLAS limit their realm of applicability to calorimeter jets with transverse momenta of at least 20 GeV [3].

However, there are important physics scenarios where the ability to identify b-hadrons with lower transverse momenta would greatly improve the analysis sensitivity.

One example is the production of the supersymmetric partners of third generation quarks (top squark or stop, $\tilde{t}_1$, and bottom squark or sbottom, $\tilde{b}_1$) with compressed mass spectra. Compressed supersymmetric scenarios [4–9], where either the stop or the sbottom is nearly mass-degenerate with the lightest supersymmetric particle (LSP), are favoured in scenarios of electroweak baryogenesis [10, 11]. The low transverse momentum (p_{T}) of the squark decay products (for instance in $\tilde{t}_1 \to bff'\tilde{\chi}^0_1$, where f and f' are generic fermions and $\tilde{\chi}^0_1$ is the lightest neutralino assumed to be the LSP, or in $\tilde{b}_1 \to b\tilde{\chi}^0_1$) makes such scenarios hard to detect. Figure 1 (a) shows that the b-hadron p_{T} spectrum peaks at 10-15 GeV (5 GeV) in simulated events with pair-produced sbottoms (stops) decaying through $\tilde{b}_1 \to b\tilde{\chi}^0_1$ ($\tilde{t}_1 \to bff'\tilde{\chi}^0_1$), where the difference in mass between the squark and the neutralino is set to $\Delta m = 20$ GeV. The softer spectrum for $\tilde{t}_1$ events is due to the four-body nature of the assumed decay. Such low-p_{T} b-hadrons are tagged by standard b-tagging algorithms based on tracks associated to calorimeter jets (see Section 4) only in a relatively small fraction of cases: although one expects two b-hadrons from the pair-produced particle decay, only 10% or less of the events have two b-tagged jets, with more than 70% of the events having no b-tagged jet at all (Figure 1 (b)).

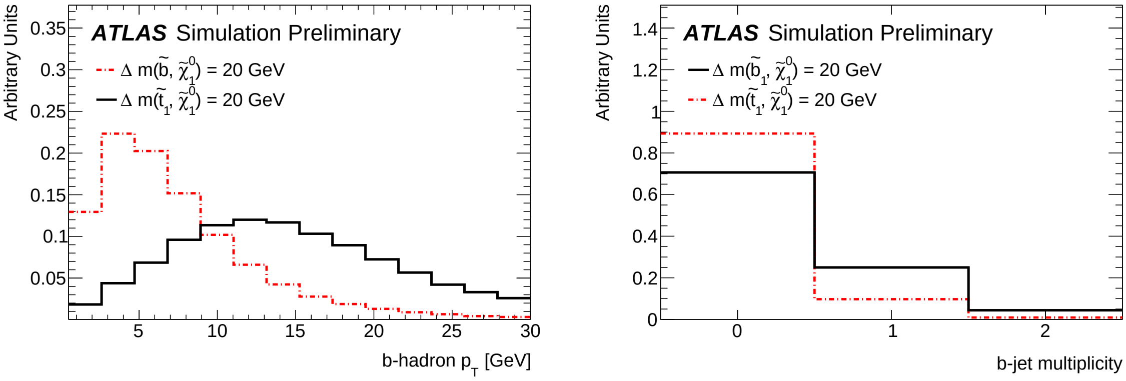

(a) (b)

Figure 1: (a) The p_{T} spectrum of generated b-hadrons produced by either $\tilde{t}_1 \to bff'\tilde{\chi}^0_1$ or $\tilde{b}_1 \to b\tilde{\chi}^0_1$ with $\Delta m = 20$ GeV. (b) The number of calorimeter jets b-tagged with the standard MV2c10 algorithm (77% efficiency working point when applied to calorimeter jets with $p_{\mathrm{T}} > 20$ GeV in simulated $t\bar{t}$ events).

The current results from the ATLAS [12–15] and CMS [16, 17] collaborations on the stop and sbottom searches reflect such behaviour: the limits on compressed scenarios are significantly less stringent than those on non-compressed scenarios [1].

The main objective of this work is to increase the sensitivity to low-p_{T} b-hadrons, by making use of two different approaches. The first approach extends standard b-tagging techniques used on jets reconstructed directly from tracks [18] to lower p_{T} compared to previous use cases, such as the search for new physics processes with Higgs boson tagging techniques [19].

In the following, this approach will be referred to as *track-jet-based b-tagging*. The second approach is not relying on the presence of any jet, but only on the presence of a secondary vertex produced by the b-hadron decay. Two different implementations of this approach have been developed. Each implementation is optimised independently for different physics scenarios, leading to different choices made during the optimisation process. The first implementation (referred to as *Track-based Low-p_T Vertex Tagger*, or *T-LVT* in the following) relies on a vertexing algorithm originally developed for the detection of long-lived particles in scenarios of new physics [20]. It has been designed to be used in compressed stop scenarios. The second implementation (*Track-Cluster-based Low-p_T Vertex Tagger*, *TC-LVT*) relies instead on a modified version of the vertexing algorithm optimised to find secondary vertices within, or in the vicinity of, a jet [21], and has been optimised for compressed sbottom scenarios.

After introducing the ATLAS detector in Section 2, the dataset and simulated event samples used in Section 3, and the final state object reconstruction in Section 4, the algorithms are introduced in Section 5. They are then characterised in terms of expected performance on simulated signal events, where genuine low-p_{T} b-hadrons are present, and background events, where no b-hadron is present in Section 6. The agreement between the simulation prediction and data on basic observables sensitive to the presence of low-p_{T} b-hadrons are also discussed in Section 7. Finally, conclusions are drawn in Section 8.

2 ATLAS detector

The ATLAS detector [22] at the LHC covers nearly the entire solid angle around the collision point.[2] It consists of an inner tracking detector surrounded by a thin superconducting solenoid, electromagnetic and hadronic calorimeters, and a muon spectrometer incorporating three large superconducting toroidal magnets. The inner-detector system (ID) is immersed in a 2 T axial magnetic field and provides charged-particle tracking in the range $|\eta| < 2.5$.

The high-granularity silicon pixel detector covers the vertex region and typically provides four measurements per track, with the first hit usually being in the insertable B-layer (IBL) installed before Run 2 [23, 24]. It is followed by the silicon microstrip tracker (SCT) which usually provides eight measurements per track. These silicon detectors are complemented by the transition radiation tracker (TRT), which enables radially extended track reconstruction up to $|\eta| = 2.0$.

---

[1] It is worth noticing that CMS is already successfully using techniques similar to T-LVT and TC-LVT in Ref. [17]

[2] ATLAS uses a right-handed coordinate system with its origin at the nominal interaction point (IP) in the centre of the detector and the z-axis along the beam pipe. The x-axis points from the IP to the centre of the LHC ring, and the y-axis points upwards. Cylindrical coordinates (r, ϕ) are used in the transverse plane, ϕ being the azimuthal angle around the z-axis. The pseudorapidity is defined in terms of the polar angle θ as $\eta = -\ln\tan(\theta/2)$. Angular distance is measured in units of $\Delta R \equiv \sqrt{(\Delta\eta)^2 + (\Delta\phi)^2}$.

Lead/liquid-argon (LAr) sampling calorimeters provide electromagnetic (EM) energy measurements with high granularity. A hadron (steel/scintillator-tile) calorimeter covers the central pseudorapidity range ($|\eta| < 1.7$). The end-cap and forward regions are instrumented with LAr calorimeters for both EM and hadronic energy measurements up to $|\eta| = 4.9$. The muon spectrometer surrounds the calorimeters and is based on three large air-core toroidal superconducting magnets with eight coils each. The field integral of the toroids ranges between 2.0 and 6.0 T·m across most of the detector. The muon spectrometer includes a system of precision tracking chambers and fast detectors for triggering.

Interesting events are selected to be recorded by the first-level trigger system implemented in custom hardware, followed by selections made by algorithms implemented in software in the high-level trigger [25]. The first-level trigger reduces the 40 MHz bunch crossing rate to below 100 kHz, which the high-level trigger further reduces to about 1 kHz before the events are written to disk.

3 Data and Monte Carlo simulated event samples

Samples of Monte Carlo (MC) simulated events are used for the optimisation of the tagging algorithms, to assess the taggers efficiency on b-hadrons, their fake rate, and finally to validate the agreement between data and MC simulation in dedicated kinematic regions enriched in b-hadrons. Details of the simulated samples used, including the matrix element (ME) event generator and parton distribution function (PDF) set, the parton shower (PS) and hadronisation model, the set of tuned parameters (tune) for the underlying event (UE) and the order of the cross-section calculation, are summarised in Table 1.

Table 1: Overview of the nominal simulated samples

Process	ME event generator	ME PDF	PS and hadronisation	UE tune	Cross-section calculation
$t\bar{t}$	Powheg-Box v2 [26]	NNPDF3.0 [27]	Pythia 8.186 [28]	A14 [29]	NNLO+NNLL [30–35]
Single-top					
t-channel	Powheg-Box v1	NNPDF3.0	Pythia 8.186	A14	NNLO+NNLL [36]
s- and Wt-channel	Powheg-Box v2	NNPDF3.0	Pythia 8.186	A14	NNLO+NNLL [37, 38]
V+jets ($V = W/Z$)	Sherpa 2.2.1 [39]	NNPDF3.0	Sherpa	Sherpa	NNLO [40]
Diboson	Sherpa 2.2.1 – 2.2.2	NNPDF3.0	Sherpa	Sherpa	NLO
$t\bar{t} + V$	MG5_aMC@NLO 2.3.3 [41]	NNPDF3.0	Pythia 8.186	A14	NLO [41]
SUSY signal	MG5_aMC@NLO 2.6.2	NNPDF2.3 [42]	Pythia 8.186	A14	NNLO+NNLL [43–45]

The samples showered with Pythia 8.186 [28] used EvtGen v1.6.0 [46] for the modelling of b-hadron decays. The signal samples were all processed with a fast simulation [47], whereas all background samples were processed with the full simulation of the ATLAS detector [47] based on GEANT4 [48]. All samples were produced with varying numbers of minimum-bias interactions overlaid on the hard-scattering event to simulate the effect of multiple pp interactions in the same or nearby bunch crossings (also referred to as pileup in the following). The number of interactions per bunch crossing was reweighted to match the distribution in data.

More details of the $t\bar{t}$, W + jets, Z + jets, diboson and $t\bar{t} + V$ samples can be found in Refs. [49–52].

The SUSY samples were generated at leading order (LO) with MG5_aMC@NLO including up to two extra outgoing partons, and interfaced to Pythia 8.186 for parton showering and hadronisation. The

$\tilde{t}_1 \rightarrow b f f' \tilde{\chi}_1^0$ samples were generated using a filter on the sum of the momenta of invisible final state particles, required to be larger than 100 GeV. The top squark was decayed with MadSpin [53], interfaced with Pythia 8.186 for the parton showering. MadSpin emulates kinematic distributions such as the mass of the bW^* system to a good approximation without calculating the full ME. For the $\tilde{b}_1 \rightarrow b\tilde{\chi}_1^0$ samples, the bottom squark was decayed in Pythia 8.186 using phase space considerations only and not the full ME.

The dataset used for the comparison of the MC predictions with data corresponds to a total of 139 $\text{fb}^{-1}$of proton-proton (pp) collision data collected by the ATLAS detector with a centre-of-mass energy of 13 TeV and a 25 ns proton bunch crossing interval in the period between 2015 and 2018. All detector subsystems were required to be operational during data taking. The average number of interactions per bunch crossing for this dataset is between 10 and 60, with a mean value of 34. The uncertainty in the combined 2015-2018 integrated luminosity is 1.7% [54], obtained using the LUCID-2 detector [55] for the primary luminosity measurements.

4 Object definition

Tracks that are reconstructed [56–58] within the inner detector must have pseudorapidy at the perigee $|\eta| < 2.5$ and $p_{\text{T}} > 0.5$ GeV, and are required to satisfy a set of quality criteria. For the track-jet-based b-tagging and TC-LVT algorithms, tracks should have at least seven hits in the silicon detectors, no more than one hit shared with other tracks in the silicon detectors, no more than one missing hit in the pixel detector, and no more than two missing hits in the SCT detector. The longitudinal impact parameter of the track with respect to the primary vertex[3] (PV) is required to satisfy $|z_0 \sin\theta| < 3$ mm. For T-LVT, tracks should have at least four hits in the pixel silicon detectors and one in the SCT detector, and satisfy $|z_0 \sin\theta| < 1.2$ mm.

The track-jet-based b-tagging algorithm makes use of variable-radius (VR) jets reconstructed from the tracks satisfying the selection above. Such jets are reconstructed using the anti-k_t algorithm [59], where the R parameter is chosen in a p_{T} dependent way [60]:

$$R \rightarrow R_{\text{eff}}(p_{\text{T}}) = \frac{\rho}{p_{\text{T}}}. \tag{1}$$

The parameter ρ defines how fast the effective jet size decreases with the p_{T} of the jet. Two additional parameters R_{min} and R_{max} are used to set, respectively, a lower and an upper cut on the jet size. The optimal values of these three parameters have been found to be: $\rho = 30$ GeV, $R_{\text{min}} = 0.02$ and $R_{\text{max}} = 0.4$ [19]. In the p_{T} regime of interest for this work ($p_{\text{T}} < 30$ GeV), this implies $R = 0.4$ for all jets. VR track jets are retained for further analysis if their p_{T} satisfies $p_{\text{T}} > 5$ GeV.

Other final state objects, such as electrons, muons, calorimeter jets and b-jets, are used to define the selection of the kinematic regions described in Section 7, where the performance of the MC simulation is compared to data.

Electron candidates are reconstructed from energy clusters in the electromagnetic calorimeter and inner-detector tracks. They are required to satisfy the *tight* likelihood identification criteria [61, 62]. Furthermore, lepton isolation, defined as the sum of the transverse energy or momentum reconstructed in a cone with a

---

[3] The selected primary vertex is the primary vertex for which the scalar sum of the squared transverse momenta of all associated tracks is the highest.

certain size ΔR excluding the energy of the lepton itself, is required. The isolation criteria rely on both track- and calorimeter-based information. Candidate electrons are required to have $p_{\mathrm{T}} > 27$ GeV and $|\eta| < 2.47$.

Muon candidates are reconstructed from matching tracks in the inner detector and muon spectrometer. They are required to meet *medium* quality and identification criteria as described in Ref. [63], and to be isolated using similar criteria as for electrons. They are required to have $p_{\mathrm{T}} > 27$ GeV and $|\eta| < 2.7$.

Calorimeter jets are reconstructed from three-dimensional topological energy clusters [64] in the calorimeter using the anti-k_t jet algorithm with a radius parameter of $R = 0.4$ [65]. Each topological cluster is calibrated to the electromagnetic scale prior to jet reconstruction. The reconstructed jets are then calibrated to the energy scale of stable final state particles in the MC simulation by a jet energy scale (JES) correction derived with $\sqrt{s} = 13$ TeV data and simulations [3]. Further selections are applied to reject jets within $|\eta| < 2.5$ that originate from pileup interactions by means of a multivariate algorithm using information about the tracks matched to each calorimeter jet [66]. Candidate calorimeter jets are required to have $p_{\mathrm{T}} > 20$ GeV and $|\eta| < 2.8$.

A calorimeter jet is tagged as a b-jet by means of the MV2c10 multivariate algorithm which uses information about the impact parameters of inner-detector tracks matched to the jet, the presence of displaced secondary vertices, the reconstructed flight paths of b- and c-hadrons inside the jet and the topology of the b-hadron decay [1, 2, 67]. Only jets with $|\eta| < 2.5$ are considered for b-tagging. Several operating points are available, corresponding to various efficiencies obtained on $t\bar{t}$ simulated events. The 77% efficiency point is used unless differently specified. This configuration corresponds to a background rejection factor of 4 for c-jets, and of 113 for light-quark and gluon jets on simulated $t\bar{t}$ events.

Overlaps between reconstructed objects are accounted for and removed based on the angular separation between different final state objects. The procedure is similar to the one described, for example, in Ref. [14].

5 Description of algorithms

5.1 Track-jet-based b-tagging

The first of the three techniques explored makes use of VR track jets. Previous work in the context of Higgs tagging techniques [19] has already used b-tagging techniques on VR track jets with $p_{\mathrm{T}} > 10$ GeV. The current work extends this further in the low-p_{T} regime, making it available for VR track jets with $p_{\mathrm{T}} > 5$ GeV. The reconstructed VR track jets are required to have at least two associated tracks. Furthermore, a veto is applied against concentric VR jets: if the ΔR distance between the axis of two VR jets is below the R size of the smallest VR jet, then the event is discarded. This procedure removes less than 1% of the events. The MV2c10 b-tagging algorithm [67] is applied to the VR jets satisfying the conditions above. Three different working points, having nominal efficiencies of 60%, 70%, 77% on a simulated $t\bar{t}$ sample are defined by selecting jets above a given threshold on the tagger discriminant distribution.

5.2 Soft vertexing

An alternative approach is to identify the presence of secondary vertices directly from the reconstructed tracks in the event, without depending on neither calorimeter nor track jets. Two similar algorithms have been developed, that rely on different vertexing techniques.

5.2.1 T-LVT

The first vertexing approach relies on an existing vertexing algorithm [20] developed in the context of the search for displaced vertices in the ID due to the decay of long-lived particles in new physics scenarios [68]. The first step is to make additional requirements on the tracks, on top of those described in Section 4. Selections are applied on the significances of z_0 and of the transverse impact parameters measured with respect to the PV, d_0 ($\frac{z_0}{\sigma(z_0)} > 0.5, \frac{d_0}{\sigma(d_0)} > 1.7$). Tracks which have $\Delta R < 0.4$ from the axis of a calorimeter jet with $p_{\mathrm{T}} > 30$ GeV are removed, both to limit the overlap with existing b-tagging techniques and to reduce the rate of fake vertices reconstructed in the dense environment within jets. From the selected tracks, a list of candidate two-track seed vertices is built: all possible two-track combinations are tested, and two-track seeds are retained based on the estimated position of the vertex candidate (the angle θ between the vector $\mathbf{r}$ pointing from the PV to the secondary vertex and the 3-vector $\mathbf{p}^{\mathrm{vtx}}$ obtained from the vectorial sum of the track momenta has to satisfy $\cos\theta > 0.7$). Then, starting from the list of two-track seeds, n-track vertices are formed ($n \geq 2$), using an incompatibility graph technique [20], followed by dedicated steps to resolve potential ambiguities arising from track association to multiple vertices. Once the final list of secondary vertices is produced, selections are applied on several observables to reject vertices which are unlikely the result of b-hadron decays. The observables used are:

- the significance of the 3D distance with respect to the primary vertex, $L_{\mathrm{3D}}^{\mathrm{sig}}$.
- the displacement in the transverse plane of the secondary vertex with respect to the primary vertex, L_{xy}.
- the angle $\theta(\mathbf{r}, \mathbf{p}^{\mathrm{vtx}})$ between the vector $\mathbf{r}$ pointing from the PV to the secondary vertex and the 3-vector $\mathbf{p}^{\mathrm{vtx}}$ obtained from the vectorial sum of the track momenta.
- the mass of the secondary vertex m_{vtx} as calculated from the associated tracks, assuming the charged pion mass for each track.
- the total transverse momentum of the tracks attached to the secondary vertex, $p_{\mathrm{T}}^{\mathrm{vtx}}$.
- the η of the secondary vertex, η_{vtx}.
- the mean angular distance ΔR_{mean} between the individual track momenta and $\mathbf{p}^{\mathrm{vtx}}$, defined as

$$\Delta R_{\mathrm{mean}} = \frac{\sum_{\mathrm{track}} \Delta R\left(\mathbf{p}^{\mathrm{track}}, \mathbf{p}^{\mathrm{vtx}}\right)}{N_{\mathrm{track}}}, \tag{2}$$

  with N_{track} being the number of tracks attached to the secondary vertex.

A *loose* and *tight* working point is defined, as summarised in Table 2. Distributions of some of these observables in signal and background samples can be found in Appendix A.

Table 2: Selections applied by T-LVT for the vertex reconstruction and identification.

Working point	$L_{\mathrm{3D}}^{\mathrm{sig}}$	L_{xy} [mm]	$\cos\theta(\mathbf{r},\mathbf{p}^{\mathrm{vtx}})$	m_{vtx} [MeV]	$p_{\mathrm{T}}^{\mathrm{vtx}}$ [GeV]	$\lvert\eta_{\mathrm{vtx}}\rvert$	ΔR_{mean}
Loose	> 5	> 0.2	> 0.9	> 600	> 3	–	< 1.0
Tight	> 7	> 0.5 and < 5	> 0.95	> 600	> 3	< 1.5	< 1.0

Table 3: Selections applied by TC-LVT for the vertex reconstruction and identification.

	Seed track		Cluster			Vertex	
Working point	$\frac{d_0}{\sigma(d_0)}$	p_{T} [GeV]	$\frac{d_0}{\sigma(d_0)}$	$\Delta R_{\mathrm{seed}}^{\mathrm{track}}$	$r_{\mathrm{seed}}^{\mathrm{track}}$ [mm]	m_{vtx} [MeV]	$p_{\mathrm{T}}^{\mathrm{vtx}}$ [GeV]
Loose	>0.5	> 1.5	> 1.5	< 0.75	< 0.25	> 600	> 3
Tight	>0.9	> 2	> 0.9	< 0.7	< 0.6	> 600	> 3

5.2.2 TC-LVT

The second vertexing approach relies instead on a vertexing technique developed in the context of standard b-tagging. Like for T-LVT, the first step is to extract a subset of displaced, relatively high-momentum tracks from the list of tracks passing the selection criteria described in Section 4. Tracks that are associated to calorimeter jets through ghost association [69] are not considered. All tracks that satisfy conditions set on the significance of the transverse impact parameter $\frac{d_0}{\sigma(d_0)}$, and on the measured transverse momentum are labelled as *seed tracks*. Seed tracks are then used to reconstruct clusters of tracks. The list of seed tracks is ordered in decreasing p_{T}. For each seed track, a cluster is formed by adding further high-d_0 significance tracks that satisfy a dedicated selection on the angular distance between the candidate and seed track $\Delta R_{\mathrm{seed}}^{\mathrm{track}}$, and on the seed-to-track distance $r_{\mathrm{seed}}^{\mathrm{track}}$, defined as the track-to-track distance of closest approach. Once tracks are associated to a cluster, they are not considered further for other clusters. The criteria used for the selection of the seed tracks and the cluster formation are specified in Table 3 for two working points of the algorithm.

The final step of the algorithm is the vertexing itself. This is done using the Single Secondary Vertex Finding algorithm (`SSVF` [21]): for each identified cluster, `SSVF` is run on all tracks in a cone of size $\Delta R = 0.4$ around the direction of the momentum sum of all tracks attached to the cluster. The main steps that `SSVF` performs on the input tracks are:

- Two-track vertices are found by looking at the spatial distance between the tracks. The rate of two-tracks vertices is suppressed by requiring that the tracks associated to the vertex do not have any hit in detector layers at a radius smaller than that of the vertex itself. Two-track vertices whose position is compatible with regions of the detector with large amounts of material are removed. Two-track vertices with invariant masses compatible with K and Λ decays are identified, and the corresponding tracks are removed if the impact parameter of the reconstructed pair is compatible with the PV. Likewise, two-track vertices with small mass under the e^+e^- hypothesis are removed to reject conversions.
- All tracks contributing to the cleaned set of two-track vertices are then combined into one list of selected tracks. This track list is supplied to the vertex fitter. The vertex fitter runs iteratively on all the tracks in the list, trying to fit one secondary vertex from all these tracks. In each iteration the

track with the largest χ^2 of the track-vertex association is removed and the vertex fit is repeated until an acceptable vertex χ^2 and a vertex invariant mass $m_{\mathrm{vtx}} < 6$ GeV are obtained.

6 Algorithms performance

After introducing the three different approaches used to identify low-p_{T} b-hadrons, their performance is evaluated using simulated events. In order to compare efficiencies and fake rates on equal footing, a common definition for the match of an object (either a VR track jet or a vertex) to generator-level particles needs to be defined. The following steps are taken to ensure such definition.

- If a b-hadron (with $p_{\mathrm{T}} > 5$ GeV for track-jet-based b-tagging and no explicit p_{T} selection for T-LVT and TC-LVT[4]) is found with a momentum vector within a cone of size $\Delta R < 0.3$ from the object's angular direction, then the object is said to be *matched to a b-hadron*. The object's angular direction is defined as the vector $\mathbf{r}_{\mathrm{vtx}}$ pointing from the PV to the secondary vertex for the vertexing algorithms, and as the jet axis for the track-jet-based b-tagging.
- Objects not matched to a b-hadron will be said to be *matched to a c-hadron* if a c-hadron with a momentum within $\Delta R < 0.3$ from the object's angular direction is found.
- Objects which are not matched to a b- or a c-hadron are classified as *unmatched*.

The fraction of b-hadrons identified with a tagged object is factorised into the fraction of b-hadrons associated to reconstructed objects (*acceptance* in the following) and the fraction of reconstructed objects matched to a b-hadron that satisfy the tagging conditions (*tagging efficiency* in the following). For the track-jet-based b-tagging, the acceptance is defined as the fraction of b-hadrons that have a VR track jet matched to them, while the tagging efficiency is defined as the fraction of objects matched to a b-hadron that pass the threshold on the value of the MV2c10 discriminant. For the vertexing algorithms, no attempt is done in this note to quote separate values for acceptance and tagging efficiency, rather only of the product of the two.

The dependence of the acceptance times tagging efficiency on the p_{T} and L_{xy} of the b-hadron can be seen in Figure 2. It is evaluated on the sample of pair-produced top squarks undergoing a four-body decay $\tilde{t}_1 \to bff'\tilde{\chi}^0_1$. The vertexing algorithms acceptance times tagging efficiency decreases at larger p_{T} as an effect of the rejection of tracks associated to calorimeter jets. The stricter track rejection criteria applied in the TC-LVT algorithm is the main reason why the loss of efficiency starts at lower p_{T} values.

The tagging efficiency and fake rates of the track-jet-based b-tagging algorithm are shown in Figure 3. The charm and light fake rates are defined as the fraction of objects matched to a c-hadron or the fraction of unmatched objects, respectively, that are tagged. Such quantities are shown as a function of the VR track jet p_{T} in Figure 3.

For the purpose of performance comparison between the three algorithms described in this note, the number of tagged objects per event matched to c-hadrons (*per-event charm fakes* in the following) or unmatched (*per-event fakes* in the following) evaluated on signal events is considered[5]. The acceptance times efficiency

---

[4] Due to the low efficiency of track-jet-based b-tagging for b-hadrons with $p_{\mathrm{T}} < 5$ GeV, this difference in threshold has no effect on the assessment of performance done in this section.

[5] For the stop sample, events where $\tilde{t}_1 \to bcs\tilde{\chi}^0_1$ or $\tilde{t}_1 \to bcd\tilde{\chi}^0_1$ are included. The average number of c-hadrons per event is about 1.7

is plotted against the number of charm fakes and fakes per event in Figure 4 in two different b-hadron p_{T} ranges.

Finally, to compare the number of per-event charm fakes and fakes on events with similar topology and for working points with similar acceptance times tagging efficiency, the following procedure is established:

- Signal events are classified in bins of p_{T} of the b-hadron. Only events that have all b-hadrons in the same p_{T} bin are retained.
- For each p_{T} bin, the working point of track-jet-based b-tagging is chosen such that the acceptance times tagging efficiency matches that of T-LVT.
- The number of per-event charm fakes and fakes is evaluated in each p_{T} bin.

The results are shown in Figure 5. The number of charm fakes and fakes per event for the vertexing algorithms at an efficiency comparable to that of track-jet-based b-tagging shows that the vertexing approach provides the best performance below a b-hadron p_{T} of about 15 GeV.

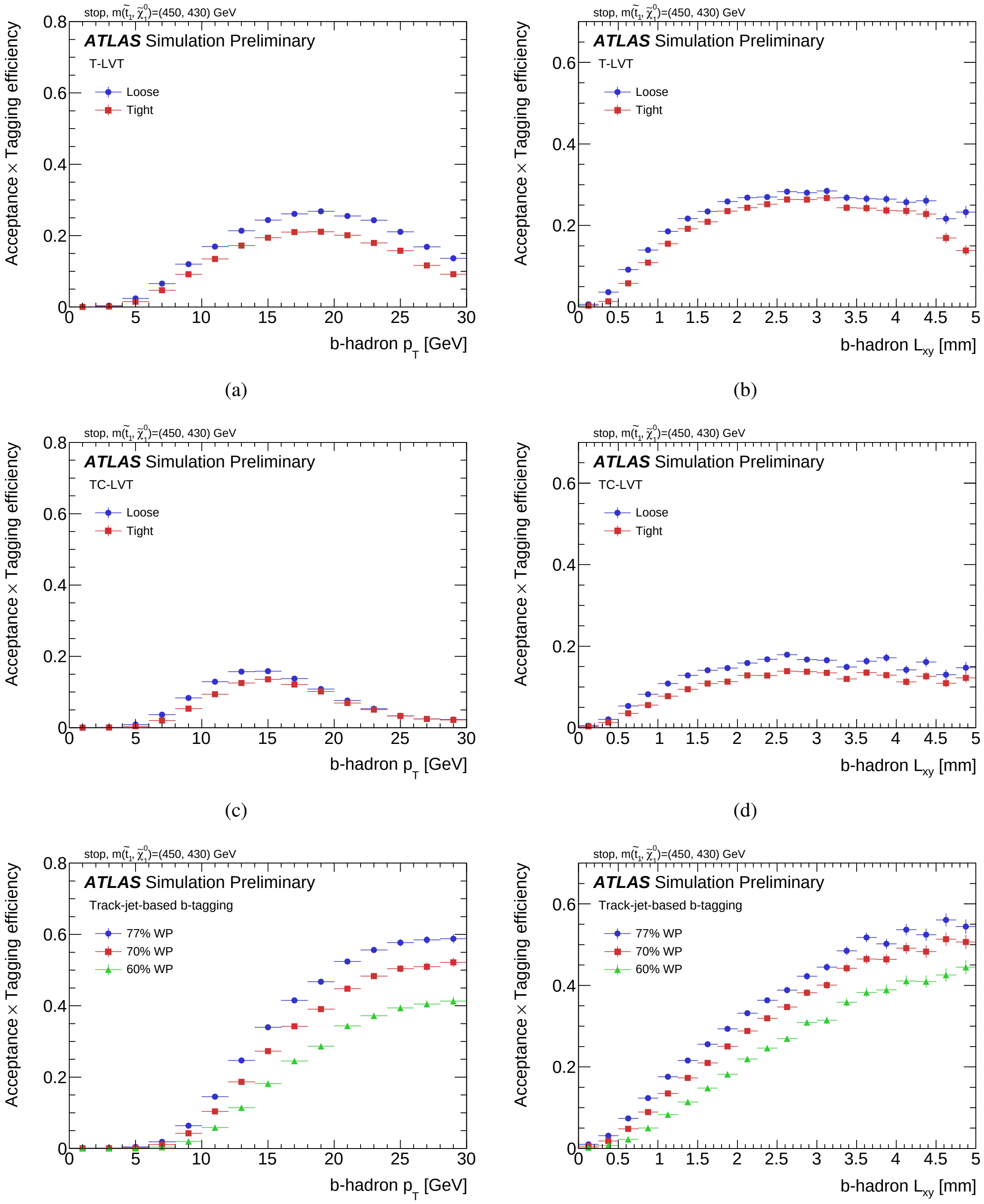

(a)

(b)

(c)

(d)

(e)

(f)

Figure 2: b-hadron acceptance times tagging efficiency as a function of (left) the b-hadron p_{T}, and (right) the distance in the transverse plane from the PV to the secondary vertex, L_{xy}. Shown are all the discussed working points of (a),(b) T-LVT, (c),(d) TC-LVT, (e),(f) track-jet-based b-tagging. All numbers are evaluated on a sample of pair-produced top squarks undergoing the four-body decay $\tilde{t}_1 \rightarrow bff'\tilde{\chi}_1^0$. The difference in mass between the $\tilde{t}_1$ and the $\tilde{\chi}_1^0$ is $\Delta m = 20$ GeV.

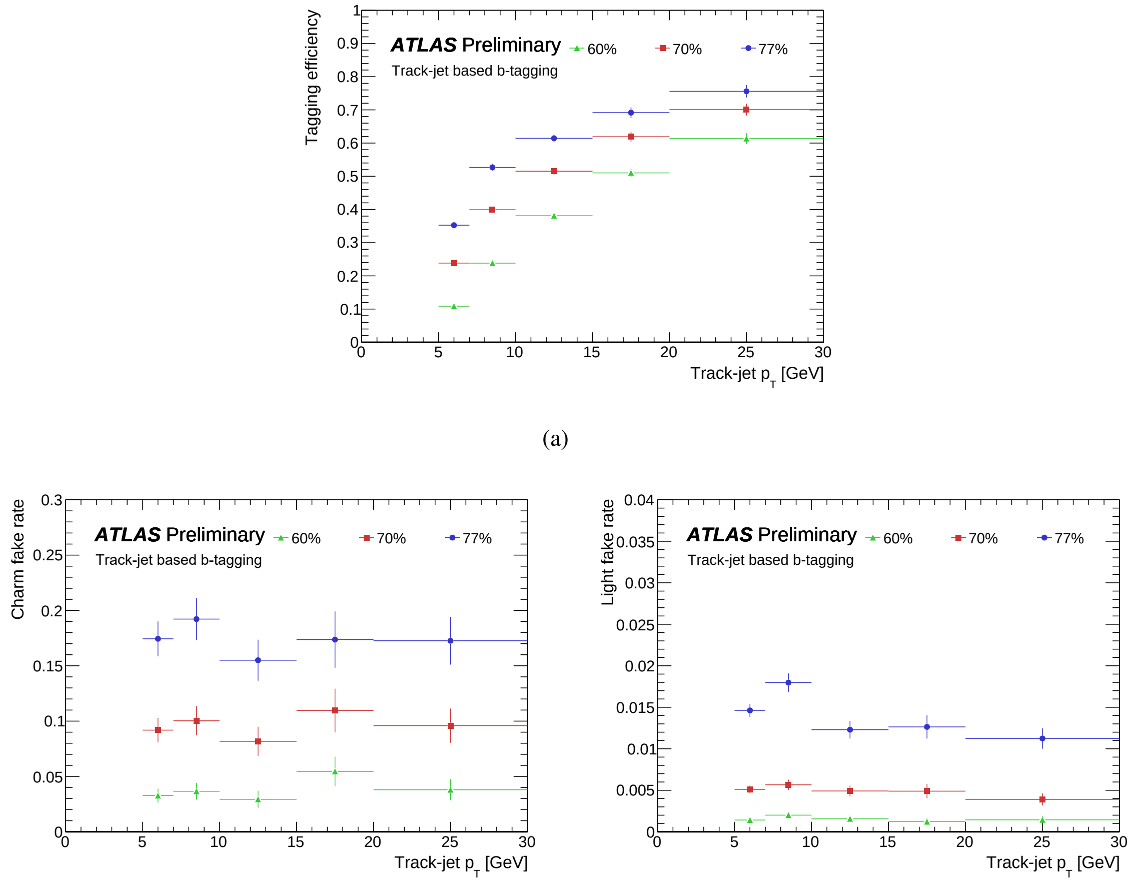

(a)

(b)

(c)

Figure 3: (a) Tagging efficiency and fraction of tagged VR tracks-jets (b) matched to a *c*-hadron (c) unmatched as a function of the VR track-jet p_{T}. The values are computed on a sample of pair-produced top squarks undergoing the four-body decay $\tilde{t}_1 \rightarrow b f f' \tilde{\chi}_1^0$ with a difference in mass between the $\tilde{t}_1$ and the $\tilde{\chi}_1^0$ of $\Delta m = 20$ GeV. The tagger used is MV2c10, and three working points are considered: 60%, 70% and 77%. The vertical error bars show the statistical uncertainty.

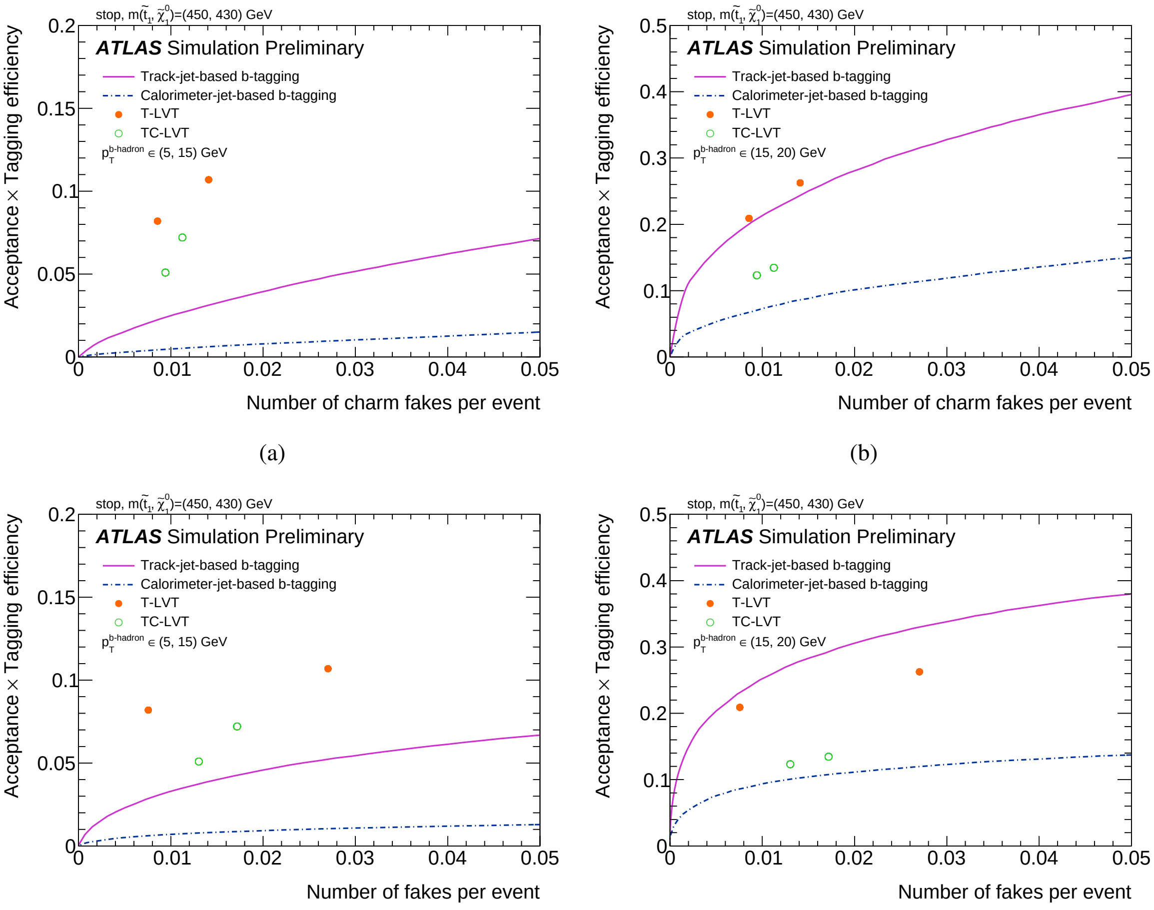

(a) (b) (c) (d)

Figure 4: Acceptance times tagging efficiency as a function of the number of charm fakes (top) or fakes (bottom) per event for the different taggers for a b-hadron p_{T} in the range 5-15 GeV (left) and 15-20 GeV (right). The loose and tight working points are shown for T-LVT and TC-LVT, while the threshold on the MV2c10 discriminant is varied for track-jet-based b-tagging. The values are computed on a sample of pair-produced top squarks undergoing the four-body decay $\tilde{t}_1 \rightarrow b f f' \tilde{\chi}_1^0$ with a difference in mass between the $\tilde{t}_1$ and the $\tilde{\chi}_1^0$ of $\Delta m = 20$ GeV.

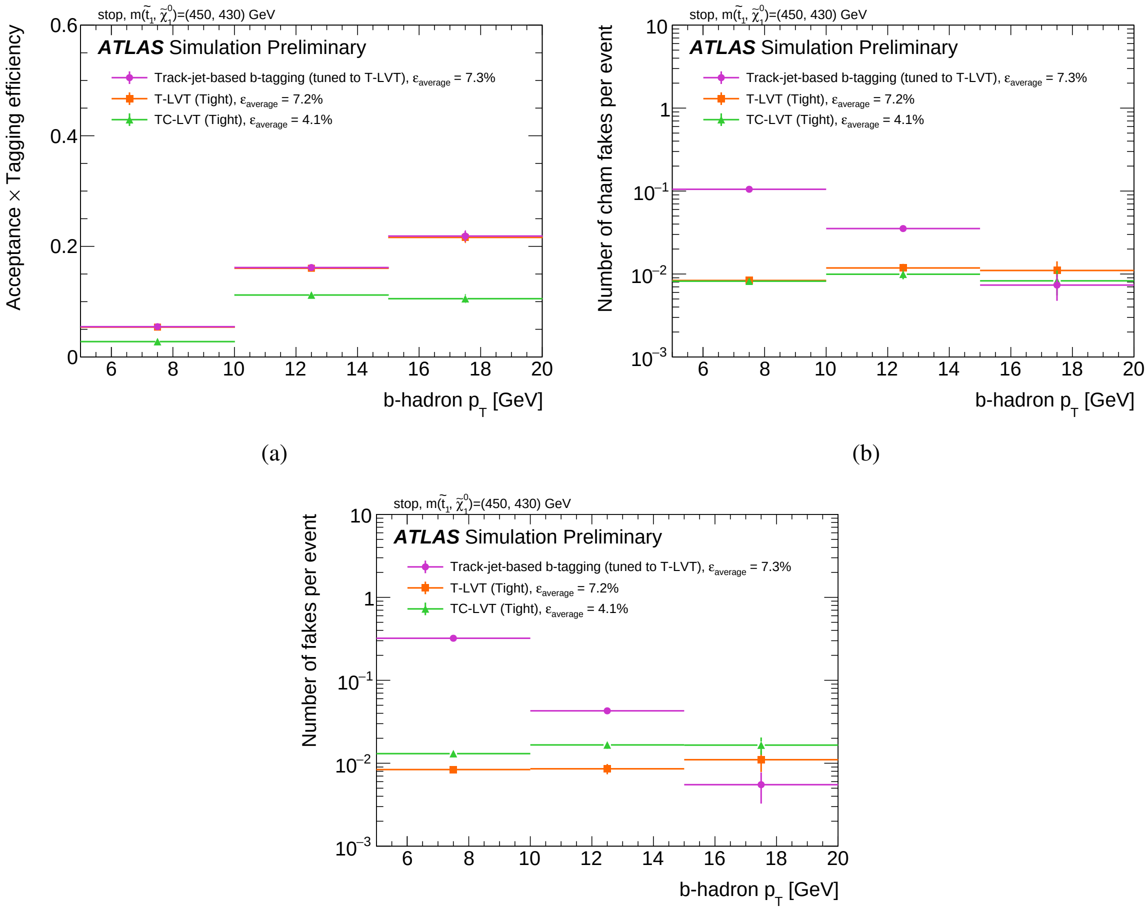

(a)

(b)

(c)

Figure 5: (a) Acceptance times tagging efficiency for the three algorithms after that of track-jet-based *b*-tagging has been tuned in each p_{T} bin to that of T-LVT, as described in the text. Number of (b) charm fakes and (c) fakes per event for the three algorithms.

7 Performance validation

It is important to assess how well the MC simulation models the properties of the tagged objects in data. For this purpose, a region in data is defined, where most of the tags are expected to come from real b-hadrons. The selection targets $t\bar{t}$ production in the dilepton final state: events are required to contain a different flavour opposite sign lepton pair ($e\mu$), at least two calorimeter jets with $p_{\mathrm{T}} > 30$ GeV, out of which one has to be b-tagged (calorimeter-jet-based b-tagging, MV2c10 with the 77% efficiency working point). This yields a sample with a $t\bar{t}$ purity above 90%.

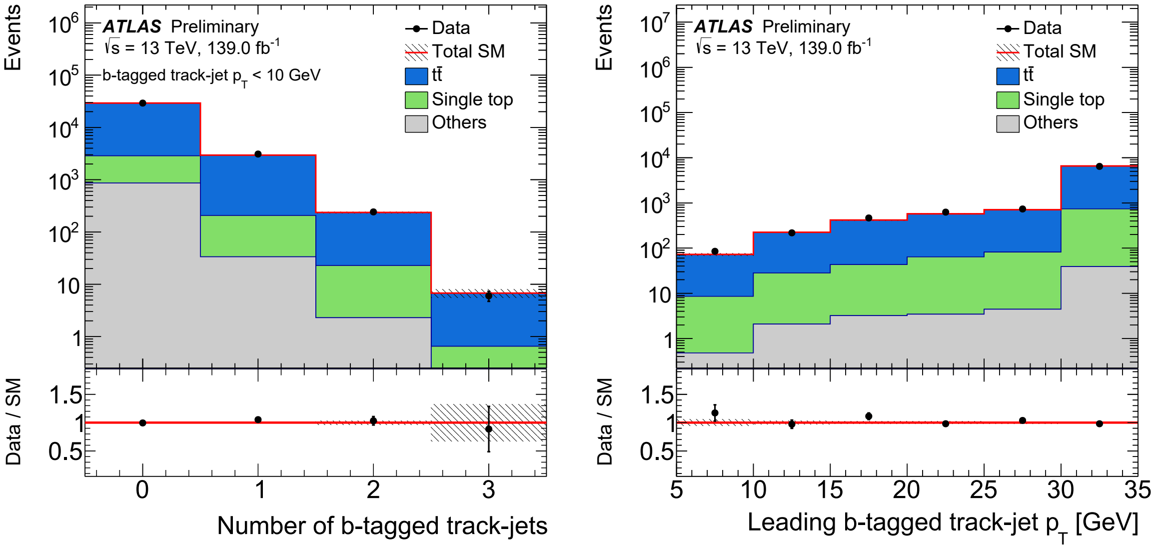

(a)

(b)

Figure 6: Comparison between data and simulated events of (a) the number of b-tagged VR track jets with $p_{\mathrm{T}} < 10$ GeV per event and (b) the p_{T} of the leading b-tagged VR track jet in a $t\bar{t}$ dominated region. The "Others" category includes contributions from V+jets, diboson and $t\bar{t} + V$ production. Ratios between data and MC simulation are reported in the lower panel. The shaded band contains the MC statistical uncertainty only. Overflow events are included in the last bin.

Figure 6 (a) shows the multiplicity of b-tagged VR track jets (MV2c10 with the 70% efficiency working point) with $p_{\mathrm{T}} < 10$ GeV for the $t\bar{t}$ selection , while Figure 6 (b) shows the p_{T} of the leading track jet. The MC simulation estimates that 98% of the tagged track jets are associated with a b-hadron when no restriction on the b-hadron p_{T} is imposed, and 91% when the $p_{\mathrm{T}} < 10$ GeV requirement is applied. Similarly, Figure 7 (a) and 8 (a) show the vertex multiplicity for T-LVT and TC-LVT, respectively. The agreement between data and MC simulation is overall reasonable. Figure 7 (b) and 8 (b) show the distribution of the vertex mass m_{vtx}. The MC simulation estimates that 93% (for T-LVT) and 95% (for TC-LVT) of the vertices are associated to b-hadrons. For the m_{vtx} distributions, the MC predictions have been rescaled to match the data yield to show the level of agreement in the shape of the distributions. The scale factor is 1.16 for T-LVT and 1.097 for TC-LVT. The detailed study and correction of these global normalisation factors will be the subject of a future work.

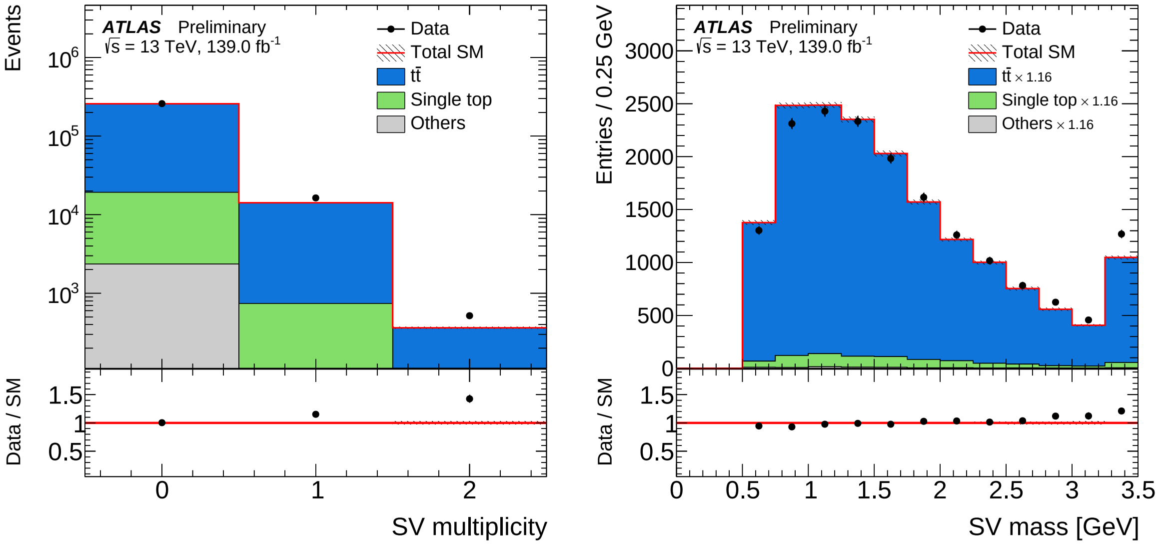

(a)

(b)

Figure 7: Comparison between data and simulated events of (a) the number of vertices per event and (b) the vertex mass for T-LVT in a $t\bar{t}$ dominated region. In (b), the MC predictions have been scaled to match the overall yield observed in data. The "Others" category includes contributions from V+jets, diboson and $t\bar{t} + V$ production. Ratios between data and MC simulation are reported in the lower panel. Overflow events are included in the last bin.

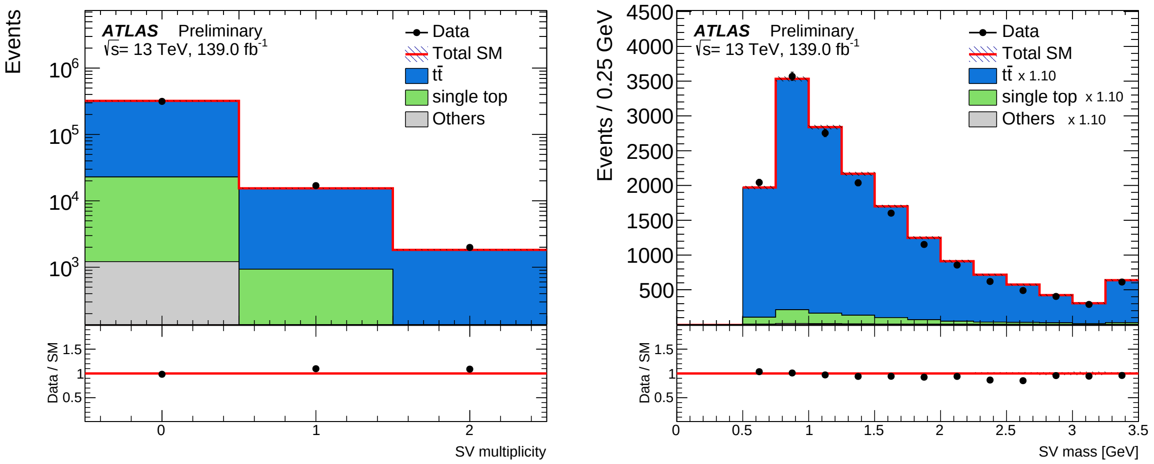

(a)

(b)

Figure 8: Comparison between data and simulated events of (a) the number of vertices per event and (b) the vertex mass for TC-LVT in a $t\bar{t}$ dominated region. In (b), the MC predictions have been scaled to match the overall yield observed in data. The "Others" category includes contributions from V+jets, diboson and $t\bar{t} + V$ production. Ratios between data and MC simulation are reported in the lower panel. Overflow events are included in the last bin.

8 Conclusions

Three different methods have been developed to improve the capability to identify low-p_{T} b-hadrons in data from the ATLAS detector. One of them relies on standard b-tagging techniques applied to jets reconstructed from tracks, while the other two aim at identifying secondary vertices produced in the b-hadron decay without relying on the presence of a jet. An evaluation of their performance shows that the methods are complementary, with the vertexing algorithms yielding the best sensitivity to b-hadrons with p_{T} in the 5-15 GeV range, and track-jet-based b-tagging performing best for $p_{\mathrm{T}} > 15$ GeV. The modelling of the tagging performance in simulation is found to be satisfactory in a data sample dominated by $t\bar{t}$ events. The tools developed in this note are expected to be particularly useful in the search for stop and sbottom production in supersymmetric models with compressed mass spectra.

A T-LVT Observable Distributions

In order to illustrate the separation power of some of the observables used by T-LVT, more information is provided in this Appendix. Figure 9 shows the distribution of the transverse impact parameter significance and the distance to the closest jet of the tracks associated to the decay of a b-hadron in the stop sample and in a sample of W-boson production where all events containing any b- or c-hadron at generator level have been removed. The figure highlights the origin of the choices for the track selection discussed in Section 4. Figure 10 shows the distribution of two of the observables used in the vertex selection by T-LVT, when all the selections on the other observables beside the one shown are applied.

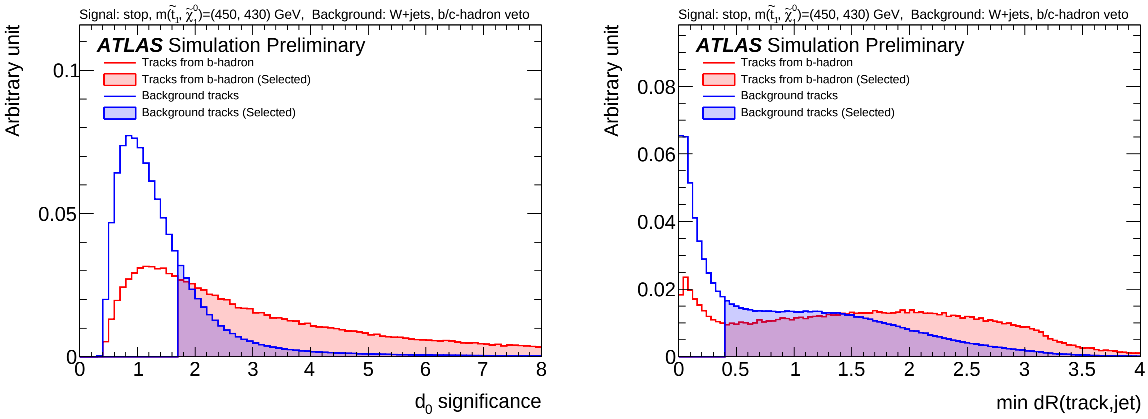

(a)

(b)

Figure 9: (a) Transverse impact parameter and (b) the minimum distance between tracks and calorimeter jets for tracks associated to the b-hadron decay in the stop sample and for tracks not associated to any b-hadron decay in a W-production sample. The shaded part of the histograms corresponds to the tracks that are accepted by the algorithm.

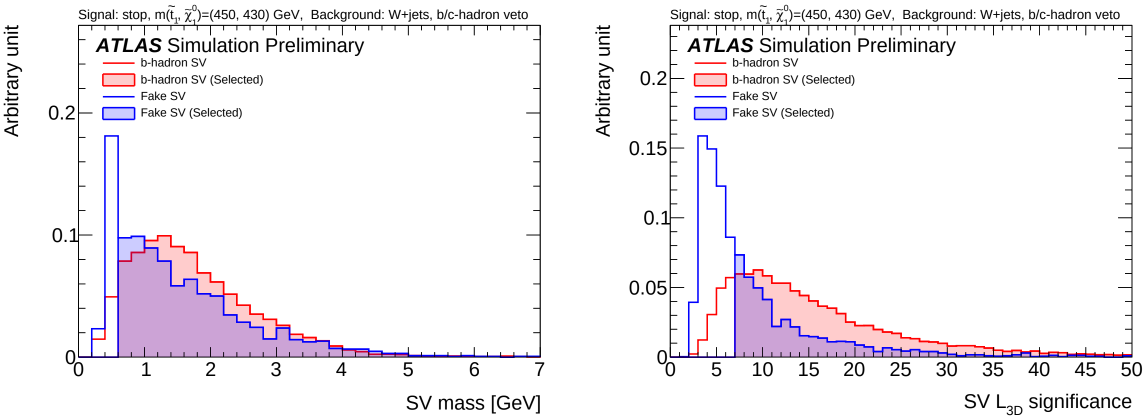

(a) (b)

Figure 10: (a) m_{vtx} and (b) L_{3D} distributions obtained by applying all vertex selections on the observables of Section 5.2.1 but that on the observable shown. The red curve refers to vertices in the stop sample while the blue one refers to a W-production sample where events containing b- or c-hadron at generator level have been removed. The shaded part of the histograms corresponds to the tracks that are accepted by the algorithm (tight working point).

References

[1] ATLAS Collaboration, *Performance of b-jet identification in the ATLAS experiment*, JINST **11** (2016) P04008, arXiv: `1512.01094 [hep-ex]`.

[2] ATLAS Collaboration, *Measurements of b-jet tagging efficiency with the ATLAS detector using $t\bar{t}$ events at $\sqrt{s} = 13$ TeV*, JHEP **08** (2018) 089, arXiv: `1805.01845 [hep-ex]`.

[3] ATLAS Collaboration, *Jet energy scale measurements and their systematic uncertainties in proton–proton collisions at $\sqrt{s} = 13$ TeV with the ATLAS detector*, Phys. Rev. D **96** (2017) 072002, arXiv: `1703.09665 [hep-ex]`.

[4] A. Golfand and E. P. Likhtman, *Extension of the Algebra of Poincare Group Generators and Violation of p Invariance*, JETP Lett. **13** (1971) 323, [Pisma Zh. Eksp. Teor. Fiz. **13** (1971) 452].

[5] D. V. Volkov and V. P. Akulov, *Is the Neutrino a Goldstone Particle?*, Phys. Lett. B **46** (1973) 109.

[6] J. Wess and B. Zumino, *Supergauge Transformations in Four-Dimensions*, Nucl. Phys. B **70** (1974) 39.

[7] J. Wess and B. Zumino, *Supergauge Invariant Extension of Quantum Electrodynamics*, Nucl. Phys. B **78** (1974) 1.

[8] S. Ferrara and B. Zumino, *Supergauge Invariant Yang-Mills Theories*, Nucl. Phys. B **79** (1974) 413.

[9] A. Salam and J. A. Strathdee, *Supersymmetry and Nonabelian Gauges*, Phys. Lett. B **51** (1974) 353.

[10] D. Delepine, J. M. Gerard, R. Gonzalez Felipe and J. Weyers, *A Light stop and electroweak baryogenesis*, Phys. Lett. **B386** (1996) 183, arXiv: `hep-ph/9604440 [hep-ph]`.

[11] D. Curtin, P. Jaiswal and P. Meade, *Excluding Electroweak Baryogenesis in the MSSM*, JHEP **08** (2012) 005, arXiv: `1203.2932 [hep-ph]`.

[12] ATLAS Collaboration, *Search for supersymmetry in final states with charm jets and missing transverse momentum in* 13 *TeV pp collisions with the ATLAS detector*, JHEP **09** (2018) 050, arXiv: `1805.01649 [hep-ex]`.

[13] ATLAS Collaboration, *Search for a scalar partner of the top quark in the jets plus missing transverse momentum final state at $\sqrt{s} = 13$ TeV with the ATLAS detector*, JHEP **12** (2017) 085, arXiv: `1709.04183 [hep-ex]`.

[14] ATLAS Collaboration, *Search for top-squark pair production in final states with one lepton, jets, and missing transverse momentum using $36\,fb^{-1}$ of $\sqrt{s} = 13$ TeV pp collision data with the ATLAS detector*, JHEP **06** (2018) 108, arXiv: `1711.11520 [hep-ex]`.

[15] ATLAS Collaboration, *Search for direct top squark pair production in final states with two leptons in $\sqrt{s} = 13$ TeV pp collisions with the ATLAS detector*, Eur. Phys. J. C **77** (2017) 898, arXiv: `1708.03247 [hep-ex]`.

[16] CMS Collaboration, *Search for top squarks decaying via four-body or chargino-mediated modes in single-lepton final states in proton–proton collisions at $\sqrt{s} = 13$ TeV*, JHEP **09** (2018) 065, arXiv: `1805.05784 [hep-ex]`.

[17] CMS Collaboration, *Search for direct production of supersymmetric partners of the top quark in the all-jets final state in proton–proton collisions at $\sqrt{s} = 13$ TeV*, JHEP **10** (2017) 005, arXiv: `1707.03316 [hep-ex]`.

[18] ATLAS Collaboration, *Flavor Tagging with Track-Jets in Boosted Topologies with the ATLAS Detector*, ATL-PHYS-PUB-2014-013, 2014, URL: `https://cds.cern.ch/record/1750681`.

[19] ATLAS Collaboration, *Variable Radius, Exclusive-k_T, and Center-of-Mass Subjet Reconstruction for Higgs($\rightarrow b\bar{b}$) Tagging in ATLAS*, ATL-PHYS-PUB-2017-010, 2017, URL: `https://cds.cern.ch/record/2268678`.

[20] ATLAS Collaboration, *Performance of vertex reconstruction algorithms for detection of new long-lived particle decays within the ATLAS inner detector*, ATL-PHYS-PUB-2019-013, 2019, URL: `https://cds.cern.ch/record/2669425`.

[21] The ATLAS Collaboration, *Secondary vertex finding for jet flavour identification with the ATLAS detector*, ATL-PHYS-PUB-2017-011, 2017, URL: `https://cds.cern.ch/record/2270366`.

[22] ATLAS Collaboration, *The ATLAS Experiment at the CERN Large Hadron Collider*, JINST **3** (2008) S08003.

[23] ATLAS Collaboration, *ATLAS Insertable B-Layer Technical Design Report*, ATLAS-TDR-19, 2010, URL: `https://cds.cern.ch/record/1291633`, Addendum: ATLAS-TDR-19-ADD-1, 2012, URL: `https://cds.cern.ch/record/1451888`.

[24] B. Abbott et al., *Production and integration of the ATLAS Insertable B-Layer*, JINST **13** (2018) T05008, arXiv: `1803.00844 [physics.ins-det]`.

[25] ATLAS Collaboration, *Performance of the ATLAS trigger system in 2015*, Eur. Phys. J. C **77** (2017) 317, arXiv: `1611.09661 [hep-ex]`.

[26] S. Alioli, P. Nason, C. Oleari and E. Re, *A general framework for implementing NLO calculations in shower Monte Carlo programs: the POWHEG BOX*, JHEP **06** (2010) 043, arXiv: `1002.2581 [hep-ph]`.

[27] R. D. Ball et al., *Parton distributions for the LHC Run II*, JHEP **04** (2015) 040, arXiv: `1410.8849 [hep-ph]`.

[28] T. Sjöstrand, S. Mrenna and P. Z. Skands, *A Brief Introduction to PYTHIA 8.1*, Comput. Phys. Commun. **178** (2008) 852, arXiv: `0710.3820 [hep-ph]`.

[29] ATLAS Collaboration, *ATLAS Pythia 8 tunes to* 7 *TeV data*, ATL-PHYS-PUB-2014-021, 2014, URL: `https://cds.cern.ch/record/1966419`.

[30] M. Czakon, P. Fiedler and A. Mitov, *Total Top-Quark Pair-Production Cross Section at Hadron Colliders Through $O(\alpha_S^4)$*, Phys. Rev. Lett. **110** (2013) 252004, arXiv: `1303.6254 [hep-ph]`.

[31] M. Czakon and A. Mitov, *NNLO corrections to top pair production at hadron colliders: the quark-gluon reaction*, JHEP **01** (2013) 080, arXiv: `1210.6832 [hep-ph]`.

[32] M. Czakon and A. Mitov, *NNLO corrections to top-pair production at hadron colliders: the all-fermionic scattering channels*, JHEP **12** (2012) 054, arXiv: `1207.0236 [hep-ph]`.

[33] P. Bärnreuther, M. Czakon and A. Mitov, *Percent Level Precision Physics at the Tevatron: First Genuine NNLO QCD Corrections to $q\bar{q} \rightarrow t\bar{t} + X$*, Phys. Rev. Lett. **109** (2012) 132001, arXiv: `1204.5201 [hep-ph]`.

[34] M. Cacciari, M. Czakon, M. Mangano, A. Mitov and P. Nason, *Top-pair production at hadron colliders with next-to-next-to-leading logarithmic soft-gluon resummation*, Phys. Lett. B **710** (2012) 612, arXiv: `1111.5869 [hep-ph]`.

[35] M. Czakon and A. Mitov, *Top++: A Program for the Calculation of the Top-Pair Cross-Section at Hadron Colliders*, Comput. Phys. Commun. **185** (2014) 2930, arXiv: `1112.5675 [hep-ph]`.

[36] N. Kidonakis, *Next-to-next-to-leading-order collinear and soft gluon corrections for t-channel single top quark production*, Phys. Rev. D **83** (2011) 091503, arXiv: 1103.2792 [hep-ph].

[37] N. Kidonakis, *Two-loop soft anomalous dimensions for single top quark associated production with a W- or H-*, Phys. Rev. D **82** (2010) 054018, arXiv: 1005.4451 [hep-ph].

[38] N. Kidonakis, *NNLL resummation for s-channel single top quark production*, Phys. Rev. D **81** (2010) 054028, arXiv: 1001.5034 [hep-ph].

[39] T. Gleisberg, S. Höche, F. Krauss, M. Schönherr, S. Schumann et al., *Event generation with SHERPA 1.1*, JHEP **02** (2009) 007, arXiv: 0811.4622 [hep-ph].

[40] S. Catani, L. Cieri, G. Ferrera, D. de Florian and M. Grazzini, *Vector boson production at hadron colliders: a fully exclusive QCD calculation at NNLO*, Phys. Rev. Lett. **103** (2009) 082001, arXiv: 0903.2120 [hep-ph].

[41] J. Alwall, R. Frederix, S. Frixione, V. Hirschi, F. Maltoni et al., *The automated computation of tree-level and next-to-leading order differential cross sections, and their matching to parton shower simulations*, JHEP **07** (2014) 079, arXiv: 1405.0301 [hep-ph].

[42] R. D. Ball et al., *Parton distributions with LHC data*, Nucl. Phys. B **867** (2013) 244, arXiv: 1207.1303 [hep-ph].

[43] M. Beneke, M. Czakon, P. Falgari, A. Mitov and C. Schwinn, *Threshold expansion of the* $gg(q\bar{q}) \rightarrow Q\bar{Q} + X$ *cross section at* $O(\alpha_s^4)$, Phys. Lett. B **690** (2010) 483, arXiv: 0911.5166 [hep-ph], Erratum: Phys. Lett. B **778** (2018) 464.

[44] M. Beneke, M. Czakon, P. Falgari, A. Mitov and C. Schwinn, Phys. Lett. B **778** (2018) 464.

[45] W. Beenakker, C. Borschensky, M. Krämer, A. Kulesza and E. Laenen, *NNLL-fast: predictions for coloured supersymmetric particle production at the LHC with threshold and Coulomb resummation*, JHEP **12** (2016) 133, arXiv: 1607.07741 [hep-ph].

[46] D. J. Lange, *The EvtGen particle decay simulation package*, Nucl. Instrum. Meth. A **462** (2001) 152.

[47] ATLAS Collaboration, *The ATLAS Simulation Infrastructure*, Eur. Phys. J. C **70** (2010) 823, arXiv: 1005.4568 [physics.ins-det].

[48] S. Agostinelli et al., *GEANT4: A Simulation toolkit*, Nucl. Instrum. Meth. A **506** (2003) 250.

[49] ATLAS Collaboration, *Simulation of top-quark production for the ATLAS experiment at* $\sqrt{s} = 13$ *TeV*, ATL-PHYS-PUB-2016-004, 2016, URL: https://cds.cern.ch/record/2120417.

[50] ATLAS Collaboration, *Monte Carlo Generators for the Production of a* W *or* Z/γ^* *Boson in Association with Jets at ATLAS in Run 2*, ATL-PHYS-PUB-2016-003, 2016, URL: https://cds.cern.ch/record/2120133.

[51] ATLAS Collaboration, *Multi-boson simulation for* 13 *TeV ATLAS analyses*, ATL-PHYS-PUB-2016-002, 2016, URL: https://cds.cern.ch/record/2119986.

[52] ATLAS Collaboration, *Modelling of the* $t\bar{t}H$ *and* $t\bar{t}V$ $(V = W, Z)$ *processes for* $\sqrt{s} = 13$ *TeV ATLAS analyses*, ATL-PHYS-PUB-2016-005, 2016, URL: https://cds.cern.ch/record/2120826.

[53] P. Artoisenet, R. Frederix, O. Mattelaer and R. Rietkerk, *Automatic spin-entangled decays of heavy resonances in Monte Carlo simulations*, JHEP **03** (2013) 015, arXiv: 1212.3460 [hep-ph].

[54] ATLAS Collaboration, *Luminosity Determination in pp Collisions at sqrt(s) = 13 TeV using the ATLAS Detector at the LHC*, ATLAS-CONF-2019-021, 2019, URL: https://cds.cern.ch/record/2677054.

[55] G. Avoni et al., *The new LUCID-2 detector for luminosity measurement and monitoring in ATLAS*, JINST **13** (2018) P07017.

[56] T. Cornelissen et al., *Concepts, Design and Implementation of the ATLAS New Tracking (NEWT)*, ATL-SOFT-PUB-2007-007, 2018, URL: `https://cds.cern.ch/record/1020106`.

[57] T. Cornelissen et al., *The new ATLAS track reconstruction (NEWT)*, J. Phys. Conf. Ser. **119** (2008) 032014.

[58] ATLAS Collaboration, *Track Reconstruction Performance of the ATLAS Inner Detector at* $\sqrt{s} = 13$ *TeV*, ATL-PHYS-PUB-2015-018, 2015, URL: `https://cds.cern.ch/record/2037683`.

[59] M. Cacciari, G. P. Salam and G. Soyez, *The anti-*k_t *jet clustering algorithm*, JHEP **04** (2008) 063, arXiv: `0802.1189 [hep-ph]`.

[60] D. Krohn, J. Thaler and L.-T. Wang, *Jets with Variable R*, JHEP **06** (2009) 059, arXiv: `0903.0392 [hep-ph]`.

[61] ATLAS Collaboration, *Electron and photon energy calibration with the ATLAS detector using 2015–2016 LHC proton–proton collision data*, JINST **14** (2019) P03017, arXiv: `1812.03848 [hep-ex]`.

[62] ATLAS Collaboration, *Electron efficiency measurements with the ATLAS detector using the 2015 LHC proton–proton collision data*, ATLAS-CONF-2016-024, 2016, URL: `https://cds.cern.ch/record/2157687`.

[63] ATLAS Collaboration, *Muon reconstruction performance of the ATLAS detector in proton–proton collision data at* $\sqrt{s} = 13$ *TeV*, Eur. Phys. J. C **76** (2016) 292, arXiv: `1603.05598 [hep-ex]`.

[64] ATLAS Collaboration, *Topological cell clustering in the ATLAS calorimeters and its performance in LHC Run 1*, Eur. Phys. J. C **77** (2017) 490, arXiv: `1603.02934 [hep-ex]`.

[65] M. Cacciari, G. P. Salam and G. Soyez, *FastJet User Manual*, Eur. Phys. J. C **72** (2012) 1896, arXiv: `1111.6097 [hep-ph]`.

[66] ATLAS Collaboration, *Performance of pile-up mitigation techniques for jets in pp collisions at* $\sqrt{s} = 8$ *TeV using the ATLAS detector*, Eur. Phys. J. C **76** (2016) 581, arXiv: `1510.03823 [hep-ex]`.

[67] ATLAS Collaboration, *Optimisation of the ATLAS b-tagging performance for the 2016 LHC Run*, ATL-PHYS-PUB-2016-012, 2016, URL: `https://cds.cern.ch/record/2160731`.

[68] ATLAS Collaboration, *Search for long-lived, massive particles in events with displaced vertices and missing transverse momentum in* $\sqrt{s} = 13$ *TeV pp collisions with the ATLAS detector*, Phys. Rev. D **97** (2018) 052012, arXiv: `1710.04901 [hep-ex]`.

[69] M. Cacciari, G. P. Salam and G. Soyez, *The Catchment Area of Jets*, JHEP **04** (2008) 005, arXiv: `0802.1188 [hep-ph]`.